Biomaterials 319 (2025) 123214

Contents lists available at ScienceDirect

Biomaterials

journal homepage: www.elsevier.com/locate/biomaterials

Biomimetic peroxisome targets myocardial injury and promotes heart repair and regeneration

Ning Zhang [a,1,*], Menghan Gao [b,1], Xiaolong Hu [c,1], Peng Wang [a], Yuan Cheng [d,e], Hui Wei [e], Guosheng Fu [a], Junbo Ge [f], Hongjun Li [g], Wenbin Zhang [a,**], Binquan Zhou [a,***]

[a] Department of Cardiology, Sir Run Run Shaw Hospital, Zhejiang University School of Medicine, Zhejiang Key Laboratory of Cardiovascular Intervention and Precision Medicine, Engineering Research Center for Cardiovascular Innovative Devices of Zhejiang Province, Hangzhou, China
[b] Department of Endocrinology, 2nd Affiliated Hospital, Zhejiang University School of Medicine, Hangzhou, China
[c] Department of Thoracic Surgery, 2nd Affiliated Hospital, Zhejiang University School of Medicine, Hangzhou, China
[d] Xishan Institute of Applied Biotechnology, Nanjing University, Wuxi, China
[e] Department of Biomedical Engineering, College of Engineering and Applied Sciences, Nanjing National Laboratory of Microstructures, Jiangsu Key Laboratory of Artificial Functional Materials, Nanjing University, Nanjing, China
[f] Department of Cardiology, Zhongshan Hospital, Fudan University, Shanghai Institute of Cardiovascular Diseases, Shanghai, China
[g] Key Laboratory of Advanced Drug Delivery Systems of Zhejiang Province, College of Pharmaceutical Sciences, Zhejiang University, Liangzhu Laboratory, Zhejiang University Medical Center, Hangzhou, China

ARTICLE INFO

Keywords:
Biomimetic
Peroxisome
Nanozyme
DDR
Heart regeneration

ABSTRACT

Heart ischemic injury predominately causes mitochondrial dysfunction, leading to the accumulation of ROS and lactate. The ROS-associated DNA damage response (DDR) contributes to myocardial cell cycle arrest and the inhibition of proliferation, while lactate accumulation is often accompanied by a high risk of acute death. In this study, to restore myocardial metabolism and regenerate the heart, we established a biomimetic peroxisome by loading the Mn_3O_4 nanozyme into mesenchymal stem cell-derived extracellular vesicles (MSC-EV (Mn@EV)). This setup mimics the peroxidases of peroxisome to catalyze ROS, and inhibit DDR. Next, the Mn@EV was immobilized with lactate oxidase (LOX) after encompassed platelet membrane to obtain biomimetic peroxisome (Mn@LPEV). This mimics the substrate-oxidizing function to detoxify lactate and prevent death. Supported by its biomimetic and lactate-response delivery system, our biomimetic peroxisome effectively targeted deep tissues in the hearts of I/R mice, achieving a 4-fold increase in targeting compared with control vesicles. It maintained myocardial redox homeostasis by scavenging ROS and lactate, inhibiting DDR pathway, promoting myocardial regeneration, reducing acute mortality and fibrosis remodeling, accelerating immunomodulation and angiogenesis, and significantly protecting heart function.

1. Introduction

Myocardial ischemic injury often occurs after coronary artery occlusion, leading to adverse outcomes such as permanent cell death and heart failure. Mechanistically, mitochondrial dysfunction-induced metabolism disorders and oxidative stress play a key role in myocardial injury and failure [1,2]. Mitochondrial dysfunction causes harmful metabolites to accumulate, leading to extensive damage. Among these factors, high lactate levels can intensify chest pain, and are often associated with a high risk of mortality during the acute phase [3–5]. Notably, ROS-induced DNA damage response (DDR) predominately contributes to myocardial cell cycle arrest [6–9], making it crucial to target this pathway to reboot the cell cycle and promote proliferation [10]. To address these issues, reestablishing redox metabolism that can decompose peroxides and catalyze lactate oxidation presents a promising approach to repair and restore the injured heart [11].

The microbody, or peroxisome, is an organelle conserved in almost all eukaryotic cells. It is filled with peroxidases and oxidases, and plays a

* Corresponding author.
** Corresponding author.
*** Corresponding author.
E-mail addresses: NingZhang17@126.com (N. Zhang), 3313011@zju.edu.cn (W. Zhang), zhoubinquan@zju.edu.cn (B. Zhou).
[1] The authors Ning Zhang, Menghan Gao and Xiaolong Hu contributed equally to this work.

https://doi.org/10.1016/j.biomaterials.2025.123214
Received 18 November 2024; Received in revised form 19 January 2025; Accepted 24 February 2025
Available online 25 February 2025

crucial role in cellular metabolism and response to oxidative stress, including substrate oxidation and maintaining redox homeostasis [12]. However, its biogenesis and cargo sorting are complex and challenging to control, making it difficult to translate into the rebuilding of myocardial metabolic function after ischemic injury [13,14]. On the contrary, artificial enzyme-like materials based on biomedical engineering, which possess redox abilities, offer promising strategies for biomimetic metabolism [15,16]. Among these, nanozymes have shown great potential of antioxidative and oxidative activities and been extensively used for therapeutic applications [17,18].

Similar to the structure of peroxisome, MSC-derived extracellular vesicles are useful for promoting revascularization after ischemia [19,20]. However, they are limited by their poor capacity to interfere DDR and promote regeneration [20,21]. Enabled by its ROS-catalyzing cascade, the Mn_3O_4 nanozyme can mimic multiple enzymes and protect cells from oxidative stress [22,23], making it attractive to attenuate myocardial DDR and reboot proliferation. To address these limitations and enhance heart regeneration, we constructed a biomimetic peroxisome in this study. The Mn_3O_4 was preloaded into MSC-EV (named Mn@EV) to mimic the antioxidant activity of peroxisomes. The vesicle surfaces were then immobilized with lactate oxidase (LOX) to catalyze the breakdown of accumulated lactate after stress. To target the heart with this artificial peroxisome (Mn@LEV), we established a platelet biomimetic peroxisome (Mn@LPEV) using a membrane fusion method [24–27]. Once cloaked with a platelet membrane, the biomimetic peroxisome can specifically target the injured vasculature in the heart.

To demonstrate proof of concept, the biomimetic peroxisome (Mn@LPEV) simultaneously reduced cellular ROS and lactate after stress and inhibited DDR, showing a synergistic effect in promoting cardiomyocyte proliferation. In a mouse myocardial I/R model, the Mn@LPEV significantly targeted injured hearts. Interestingly, the immobilized LOX not only oxidized lactate but also provided tropism towards deeply-wounded tissues. Delivered by the biomimetic and lactate-responsive system, our artificial peroxisome successfully rebuilt myocardial metabolism that remodeled redox and lactate homeostasis, mitigated myocardial DDR, and rebooted cell regeneration. Additionally, it promoted angiogenesis, modulated inflammation, and alleviated fibrosis remodeling, collectively leading to significant preservation of heart function.

2. Results

2.1. Fabrication and characteristics of the biomimetic peroxisome Mn@LPEV

To address the metabolic issues following ischemic injury, we established an artificial peroxisome with the targeted delivery system. First, the Mn_3O_4 nanozyme was synthesized [23] to mimic the peroxidase activity of peroxisomes, and then cultured with mesenchymal stem cells (MSC) to isolate Mn_3O_4-loaded MSC-EVs (Mn@EV). After that, Mn@EV was fused with platelet membrane vesicles (PMVs) before modifying with LOX, so as to detoxify lactate and facilitate delivery of our therapy, resulting in a ROS- and lactate-dual-catalyzing biomimetic peroxisome (Mn@LPEV).

The TEM analysis revealed that Mn_3O_4 nanoparticles have a size of approximately 20 nm (Fig. S1a). These nanoparticles demonstrated antioxidant properties by markedly reducing mitochondrial ROS (mROS) in P1 neonatal cardiomyocytes (P1CMs) under oxidative stress (Figs. S1b–d), as well as decreasing total cellular ROS (tROS) (Figs. S1e and f). Additionally, Mn_3O_4 protected key mitochondrial functions, including the permeability transition pore (mPTP) and membrane potential (MMP), during H_2O_2 exposure (Figs. S1g–j). As a result, Mn_3O_4 preserved the proliferative capacity of P1CMs, which was otherwise impaired by H_2O_2, as evidenced by the expression of proliferation markers Ki67 in the late G1-M phase and phosphorylated histone H3 (pH3) in the G2-M phase (Figs. S1k–n). These findings indicate that Mn_3O_4 can mimic peroxisomes by scavenging ROS, thereby promoting cell proliferation.

Once fabricated, the biomimetic peroxisome Mn@LPEV was observed under TEM, showing a morphology similar to MSC-EV, and encapsulated Mn_3O_4 nanoparticles (Fig. 1a). Proteins presentation as identified by Western Blot (WB) confirmed that typical platelet and EV maker proteins were successfully transferred to Mn@LPEV (Fig. 1b). Membrane fusion between MSC-EV and PMVs was verified by fluorescence colocalization under confocal, showing that the two samples merged after fabrication process rather than direct mixing (Fig. 1c). To confirm the incorporation of LOX and Mn_3O_4 into Mn@LPEV, Cy3-LOX and FITC-Mn_3O_4 were used to prepare Mn@LPEV, which was then applied to H9C2 cells. Cellular uptake was observed and displayed colocalization of the two fluorescent signals, demonstrating successful drug loading of Mn@LPEV (Fig. 1d). Ultimately, the size and Zeta-potential of Mn@LPEV were measured, revealing that incorporation of PMVs slightly increased the membrane potential of Mn@EV to a level closer to PMVs (Mn@EV vs. Mn@PEV vs. Mn@LPEV, -25 ± 3.5 mV vs. -19 ± 1.4 mV vs.-19 $\pm$ 0.98 mV, Fig. 1e), and suggests that the membrane content was substantially altered. The average size of Mn@EV, Mn@PEV and Mn@LPEV were 130 $\pm$ 3 nm, 120 $\pm$ 2 nm and 122 $\pm$ 3 nm, respectively (Fig. 1f).

Finally, these formulations were used to treat H9C2 to determine if the biomimetic peroxisome functioned as intended. When exposed to H_2O_2, total cellular (Fig. 1g and h) and mitochondrial ROS (Fig. 1i–k) surged but were significantly scavenged by Mn@LPEV. Meanwhile, cellular lactate significantly accumulated after stress but was detoxified by the LOX-functionalized Mn@LPEV, unlike Mn@EV, highlighting the substrate oxidation-mimicking capability of Mn@LPEV (Fig. 1l and m). In together, these results demonstrated the peroxidase and oxidase dual-mimicking activities of our fabricated biomimetic peroxisome Mn@LPEV in this study.

2.2. Mn@LPEV inhibits cardiomyocytes DDR and promotes proliferation

Mitochondrial ROS-induced DDR activation can adversely affect the myocardial cell cycle and arrest proliferation. To address this, we investigated whether the biomimetic peroxisome Mn@LPEV could inhibit myocardial DDR and promote proliferation. Upon treatment with Mn@LPEV, a significant reduction in myocardial nuclear ROS was observed following hypoxic-reoxygenation injury (H/R) (Fig. 2a and b). Consequently, there was a significant alleviation in DNA damage, as was indicated by the decrease in 8-hydroxydeoxyguanosine (8-OHdG) after Mn@LPEV treatment (Fig. 2c). Following DNA damage, repair mechanisms are initiated, during which ATM activation (pATM) plays a critical role in controlling the cell cycle [6,8,10]. In this study, Mn@LPEV treatment resulted in a significant inhibition of DDR (Fig. 2d and e), and demonstrated the essential role of Mn_3O_4 within the biomimetic peroxisome in reducing ROS accumulation and DNA damage after stress. Following the DDR pathway, check point kinase1 (CHK1) is activated leading to the phosphorylation of Wee1, which negatively regulates the cell cycle by inhibiting cyclin-dependent kinase1 (CDK1) [28,29]. Western blot analysis demonstrated that the biomimetic peroxisome Mn@LPEV inhibited Wee1 activation, and indicated its potential to maintain the myocardial cell cycle (Fig. 2f and g).

As a result, we explored cell proliferation following treatments. Notably, P1CMs treated with the biomimetic peroxisome Mn@LPEV maintained cell cycle progression and proliferation even under stressed conditions (Fig. 2h and I; Figs. S2a and b). Additionally, gene expression analysis of markers associated with fetal and neonatal stages revealed that Mn@EV and Mn@LPEV treatments increased the expression of *Acta1, Nppa, Nppb,* and *Myh7* in P7CMs. In contrast, genes associated with myocardial maturation and differentiation, including *Tnni3*, *Mylk3*, *Myocd,* and *Cacna1g* were suppressed in Mn@EV and Mn@LPEV-treated P7CMs (Fig. 2j). This suppression was further confirmed by the quantification of Cyclin E1 protein (Fig. 2k). Under our conditions, the

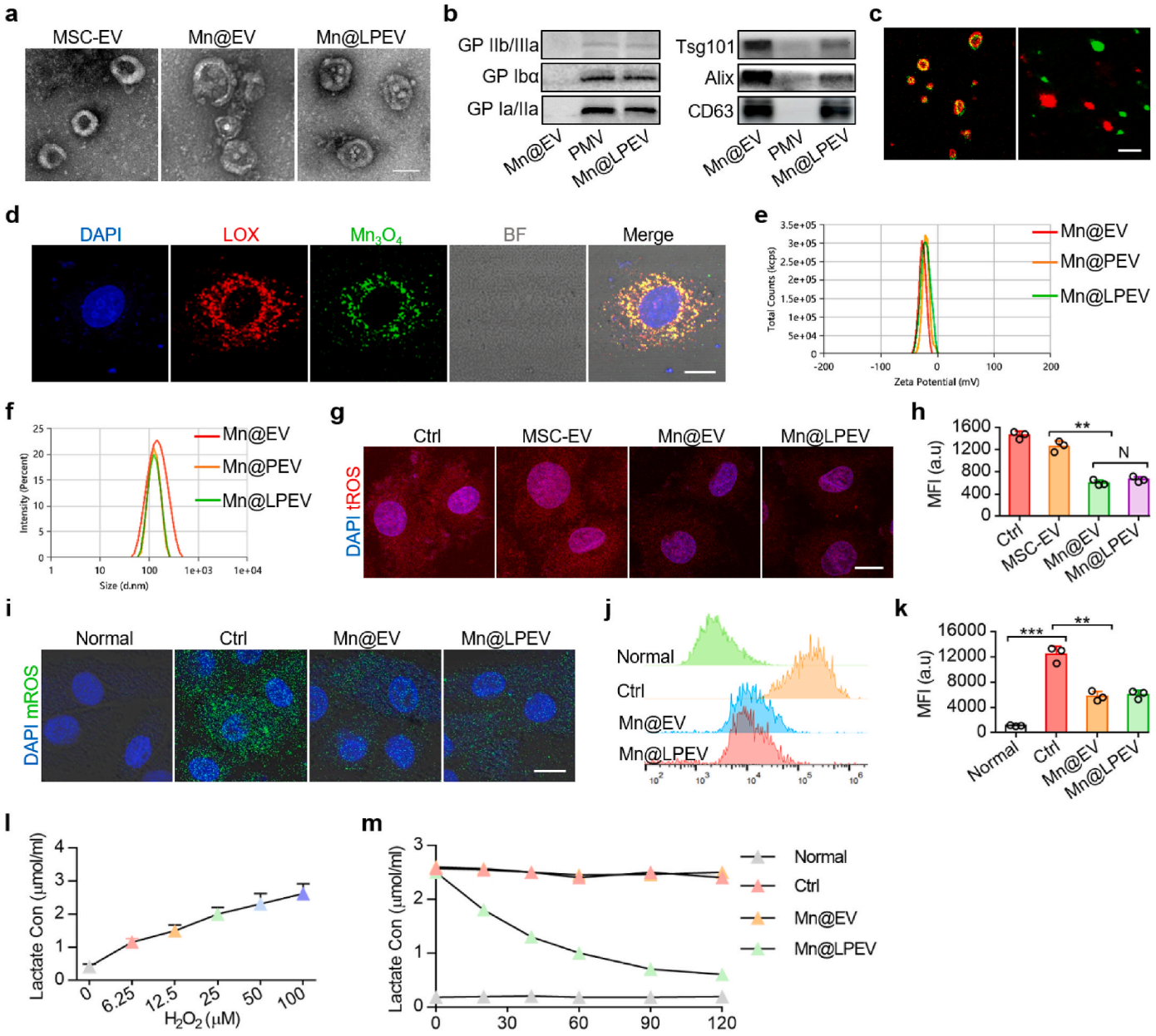

Fig. 1. Preparation and characteristics of the biomimetic peroxisome Mn@LPEV. a) TEM of MSC-EV (left), Mn@EV (middle) and Mn@LPEV (left). b) Western blot analysis verified the presence of typical proteins of platelet membrane (GPIIb/IIIa, GPIbα, GPIa/IIa) and EV (Tsg101, Alix, CD63) on Mn@EV, PMV, and Mn@LPEV. c) Confocal revealed fluorescence colocalization of Mn@PEV (left) and the direct mixture of Mn@EV and PMV (right). bar = 1 μm. d) Confocal fluorescence colocalization confirmed the loading of Mn_3O_4 and LOX within Mn@LPEV. Green, Mn_3O_4; Red, LOX. bar = 20 μm. e, f) ζ potential (e) and size (f) analysis of Mn@EV, Mn@PEV and Mn@LPEV by the DLS. n = 3. g, h) Total cellular ROS in cardiomyocytes following oxidative stress and respective treatments was indicated and quantified by DCFH probe. bar = 10 μm, n = 3. i-k) Mitochondrial ROS in cardiomyocytes following oxidative stress and respective treatments was indicated by mitoSOX probe and quantified by flowcytometry. bar = 10 μm, n = 3. l, m) Cardiomyocytes lactate levels under indicated H_2O_2 were measured (l); and when maintained under 50 μM H_2O_2 with or without respective treatments, lactate accumulation in the medium was also measured (m). n = 3. **p < 0.01, ***p < 0.001, N = non-significant.

proportion of proliferative P7CMs was also assessed. The number of Ki67-, pH3-, and AuroB-positive cardiomyocytes, indicators of mitosis, increased in cells treated with Mn@EV and Mn@LPEV-treated cells (Fig. 2m and n; Figs. S2c and d). These results demonstrate that our biomimetic peroxisome could alleviate DNA damage, inhibit the DDR/Wee1 pathway, and further promote myocardial cell cycle reentry and proliferation.

2.3. Mn@LPEV modulates immunity, promotes neovascularization

MSC-EV has been demonstrated to be effective in modulating immune and inflammation responses, and promoting angiogenesis in heart repair [19]. In this study, the immunoregulatory effects of our MSC-EV-based biomimetic peroxisome were investigated by measuring macrophage gene expression after treating inflamed RAW264.7 cells. The results showed that Mn@LPEV and Mn@EV suppressed the expression of inflammatory macrophages (M1)-related genes while increasing the expression of anti-inflammatory M2-associated genes (Fig. S3a). Consistently, the level of inflammatory cytokines, such as IL-6 and MCP-1, in the supernatants, decreased when treated with Mn@LPEV or Mn@EV (Fig. S3b). The impact of the biomimetic peroxisome Mn@LPEV on endothelial angiogenesis was also explored using

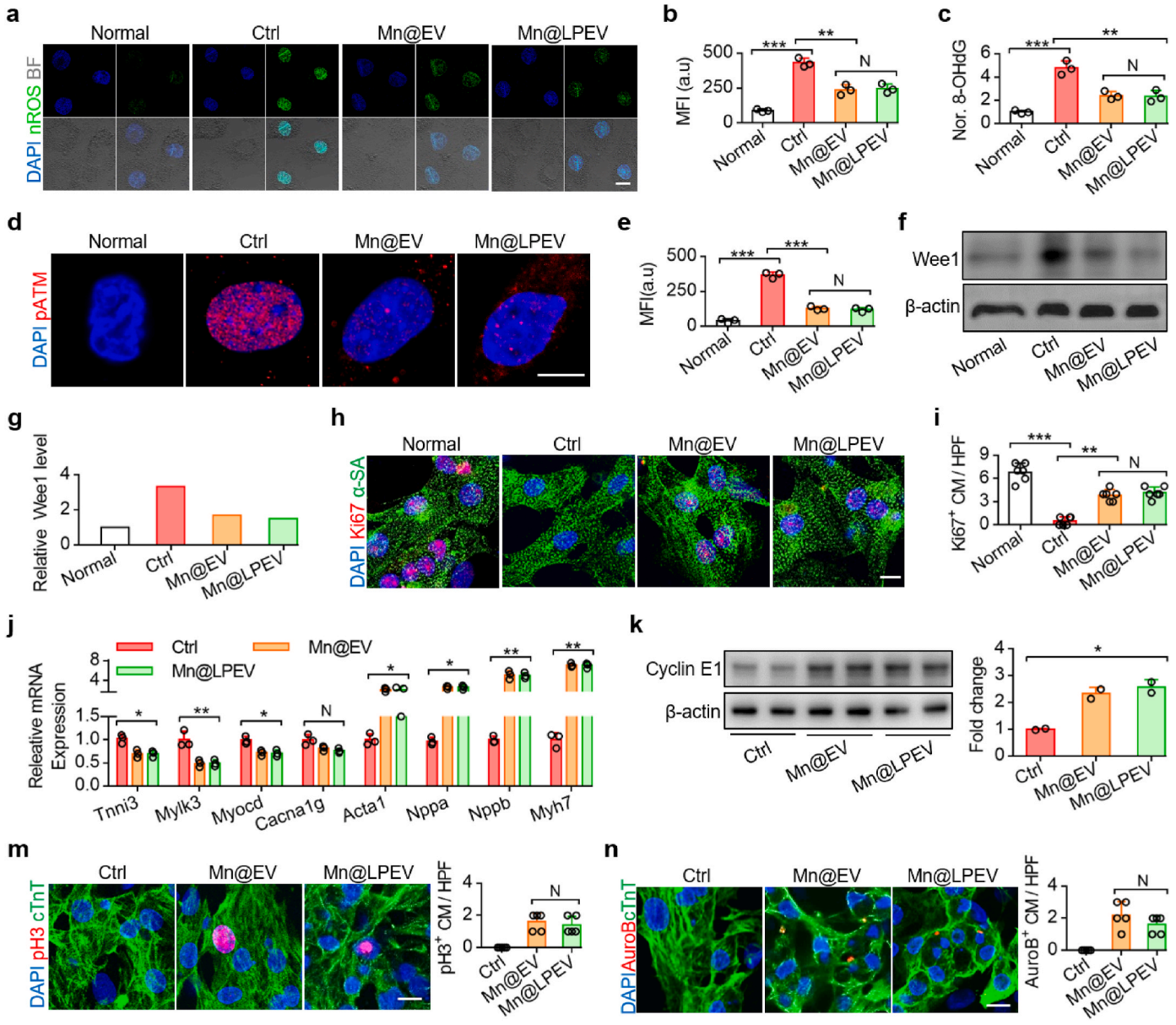

Fig. 2. Mn@LPEV inhibits cardiomyocytes DDR and promotes proliferation. a, b) The P1CM nuclear ROS after stress and treatments was indicated by DCFH after excluding cytoplasmic signal. bar = 10 μm, n = 3. c) Cellular DNA damage following stress and treatments was assessed by quantifying 8-OHdG. n = 3. d, e) Cardiomyocyte DDR was measured by immunofluorescence staining of pATM protein. Red, pATM. bar = 10 μm, n = 3. f, g) Western blot analysis was employed to measure relative expression of Wee1 vs. β-actin. h, i) P1CM proliferation was measured by immunofluorescence staining of Ki67. bar = 10 μm, n = 3. j) Relative gene expression associated with myocardial fate in P7CM after treatments was quantified by RT-qPCR. n = 3. k) Expression of cell cycle protein Cyclin E1 in P7CM was quantified by WB. n = 2. m, n) Cell proliferation indictor pH3 (m) and Auro B (n) was further measured in P7CM after respective treatments by immunofluorescence staining. bar = 10 μm, n = 3. *p < 0.05, **p < 0.01, ***p < 0.001, N = non-significant.

Matrigel assay. After treatment with Mn@LPEV or Mn@EV, the tube formation of HUVECs (ECs) was observed and quantified, demonstrated a significant increase in newly formed microvessels (Figs. S3c and d). Altogether, these results demonstrate that along with maintaining myocardial redox hemostasis and proliferation, our fabricated biomimetic peroxisome Mn@LPEV inherited the immunomodulating and pro-neovascularizing effects from MSC-EV.

2.4. Mn@LPEV targets injured tissues after myocardial I/R injury

To enhance drug delivery to deep tissues in damaged hearts, we validated the targeting capability of our biomimetic peroxisome delivery system. Initially, upon exposure to H_2O_2, an upregulation of endothelial (ECs) adhesive molecule von Willebrand factor (vWF) was observed. Consistently, the Mn@LPEV, rather than Mn@EV, showed significant binding to ECs and colocalization with vWF (Fig. 3a and b), indicating that the platelet biomimetic Mn@LPEV possesses the capability to target damaged vascular. Inspired by a previous study [30], we further investigated whether Mn@LPEV could respond to lactate and exhibit tropism toward deep tissues. We first established a tracking system where one side chamber contains lactate medium and the other side contains control medium, while the middle chamber was filled with Mn@PEV or Mn@LPEV. We observed that LOX-functionalized Mn@LPEV exhibited a tropism towards the lactate. In contrast, Mn@PEV did not exhibit any direct motion under our conditions (Fig. 3c and d). A Transwell assay was then conducted, with HUVECs in the upper and H9C2 cells in the lower chamber, both pretreated with H_2O_2 (Fig. 3e). When the upper chamber was replenished with these drugs,

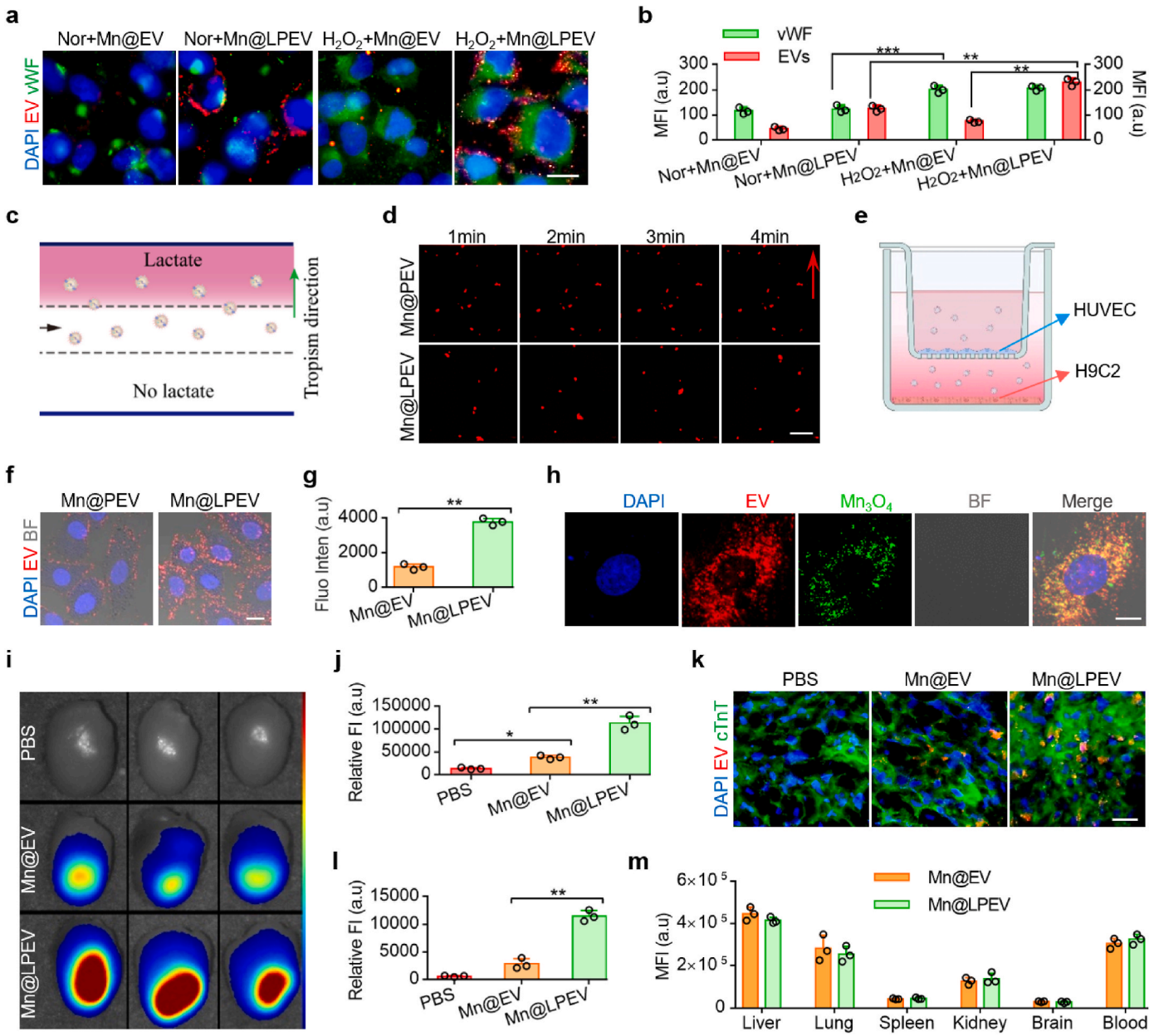

Fig. 3. Mn@LPEV targets to myocardial injury in vitro and in vivo. a, b) The Mn@EV and Mn@LPEV binds to stressed HUVEC was observed and the Mn@LPEV showed colocalizations with vWF. Green, vWF; Red, Mn@EV or Mn@LPEV. bar = 20 μm, n = 3. c) Graphical construction of the tracking system. Black arrow: the middle chamber was filled with Mn@PEV or Mn@LPEV. Green arrow: tropism direction of formulations. d) Motion tracking images of Mn@PEV and Mn@LPEV under microscope at indicated times. Red arrow: motion direction. bar = 1 μm. e-g) Scheme of the Transwell construction (e), and the internalization of Mn@PEV or Mn@LPEV by H9C2 was observed under confocal (f) and quantified (g). h), Colocalization of Mn_3O_4 and respective vesicles after internalization under confocal. Green, Mn_3O_4; Red, EVs. bar = 20 μm. i, j) Targeted accumulation of Mn@EV and Mn@LPEV in the hearts after I/R was assessed by IVIS (i) and fluorescence quantification (j). n = 3. k, l) The distribution of these formulations in heart tissue sections was observed and quantified. Red, EVs; Green, cTnT. bar = 20 μm, n = 3. m) Biodistribution of formulations in major organs and blood. n = 3. *p < 0.05, **p < 0.01, ***p < 0.001.

H9C2 cells internalized Mn@LPEV at a significant higher rate than Mn@PEV (Fig. 3f and g). Additionally, the colocalization between Mn_3O_4 and EVs within cells further confirmed the successful delivery of these drugs (Fig. 3h). This supports the conclusion that Mn@LPEV could bind to activated endothelium and subsequently move as a bioswimmer toward subendothelial tissues.

As a proof of concept, these samples were administrated intravenously to mice 24h after I/R. In vivo imaging systems (IVIS) and fluorescence quantitation demonstrated that both Mn@EV and Mn@LPEV accumulated in injured hearts. Notably, the targeting efficiency of biomimetic peroxisome Mn@LPEV was significantly higher than that of Mn@EV (2.7-fold) (Fig. 3i and j). Tissue sections were further analyzed revealing that Mn@LPEV predominately targeted injured zones with a 4-fold increase compared with Mn@EV (Fig. 3k and l). The distribution of vesicles across different organs was then assessed, demonstrating that both Mn@EV and Mn@LPEV exhibited similar distribution patterns in major organs and blood, but the Mn@LPEV group showed a trend of lower accumulation in liver and lung, which is probably attributed to the reduced mononuclear phagocyte system (MPS)-related effects caused by platelet membrane decoration (Fig. 3m). Additionally, the pharmacokinetics of platelet biomimetic Mn@LPEV was further investigated after i.v. administrated to mice via the tail vein and blood was collected at predetermined timepoints. As shown in Fig. S4, Mn@LPEV presented a relatively longer circulation time than unmodified Mn@EV, which

might be due to the "self-recognition" protein on platelet membranes as previously mentioned. Altogether, these results demonstrate that the biomimetic peroxisome Mn@LPEV effectively targets deep-injured myocardial tissues in a platelet-biomimetic and lactate-responsive manner.

2.5. Mn@LPEV alleviates myocardial injury and DDR in the I/R model

To examine the therapeutic effects of our biomimetic peroxisome in vivo, we established mice I/R models and administrated Mn@LPEV. We first assessed myocardial ROS accumulation in heart tissues 7 days after I/R. Results indicated that Mn@EV reduced ROS levels in the heart, while the biomimetic peroxisome Mn@LPEV significantly enhanced this effect (Fig. 4a and b). Consequently, Mn@LPEV protected mitochondrial morphology and increased mitochondrial quantity, showing a higher density of mitochondrial cristae (Fig. 4c and d). Cardiomyocyte apoptosis was evaluated by the Tunel assay, which showed that cell apoptosis was significantly reduced by the biomimetic peroxisome, demonstrating the myocardial protection effects of Mn@LPEV (Fig. 4e and f). Additionally, DNA damage and DDR were assessed using 8-OHdG

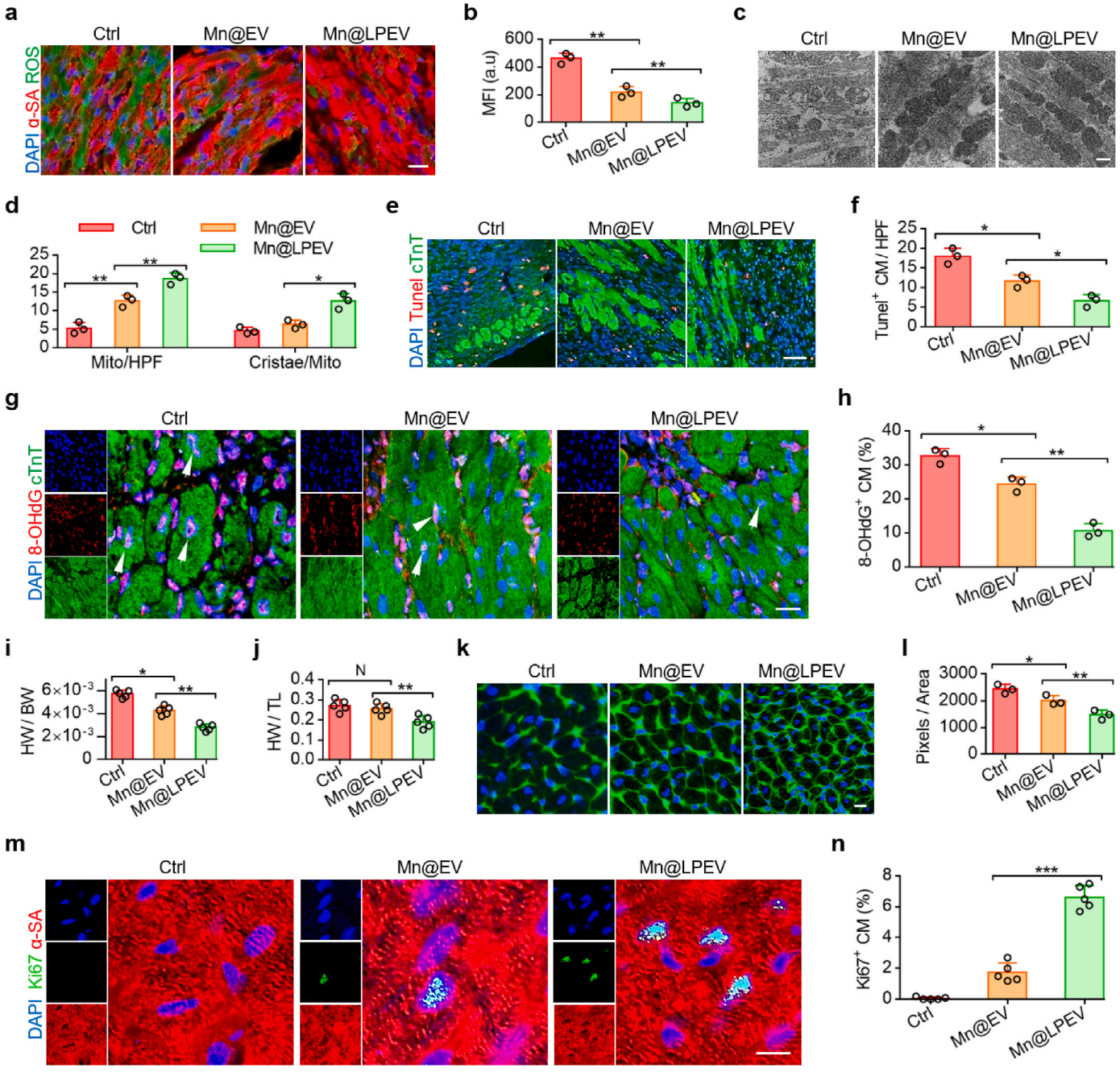

Fig. 4. Mn@LPEV alleviates myocardial DDR and promotes regeneration after I/R injury. a, b) Myocardial ROS was indicated by DHE probe and quantified 7d after I/R and treatments. Green, ROS; Red, α-SA. bar = 20 μm, n = 3. c, d) Mitochondrial damage under TEM (c) and measurement of mitochondrial cristae density (d). bar = 0.5 μm, n = 3. e, f) Cardiomyocyte apoptosis was assessed by the Tunel assay. Green, cTnT; Red, Tunel. bar = 20 μm, n = 3. g, h) Myocardial DNA damage was measured by immunostaining of 8-OHdG (g) and quantification (h). Green, cTnT; Red, 8-OHdG. bar = 20 μm, n = 3. i, j) 4 weeks after treatments, the ratio of heart weight to body weight (i) and heart weight to tibial length (j) were measured respectively. n = 5. k, l) The cellular size of cardiomyocytes was indicated (k) and measured (l) by WGA staining. Green, WGA. bar = 50 μm, n = 3. m, n) Myocardial proliferation was identified (m) and quantified (n) by Ki67. Green, Ki67; Red, α-SA. bar = 20 μm, n = 5. *p < 0.05, **p < 0.01, ***p < 0.001.

and pATM (Fig. 4g and h; Figs. S5a and b), and revealed that Mn@LPEV effectively attenuated both DNA damage and DDR after I/R. These findings indicate that consistent with cellular experiments, Mn@LPEV performs effectively in alleviating myocardial oxidative stress and DNA damage response in vivo.

2.6. Mn@LPEV promotes heart regeneration after I/R injury

28 days after I/R, we evaluated the ratio of heart weight to body weight and heart weight to tibial length. The biomimetic peroxisome Mn@LPEV effectively prevented myocardial hypertrophy compared to other treatments (Fig. 4i and j). Regarding cell morphology, WGA staining was conducted to examine variations in cell size among experimental groups. The results demonstrated a significant decrease in cell volume following the therapy of Mn@LPEV (Fig. 4k and l). As confirmed by immunolocalization (Fig. 4m and n; Figs. S5c and d), there was a significant increase in Ki67-and pH3-positive cardiomyocytes in Mn@LPEV-treated hearts. This demonstrates that Mn@LPEV facilitate cardiomyocyte reentry into the cell cycle and promotes myocardial regeneration after I/R. Based on these findings, we have corroborated

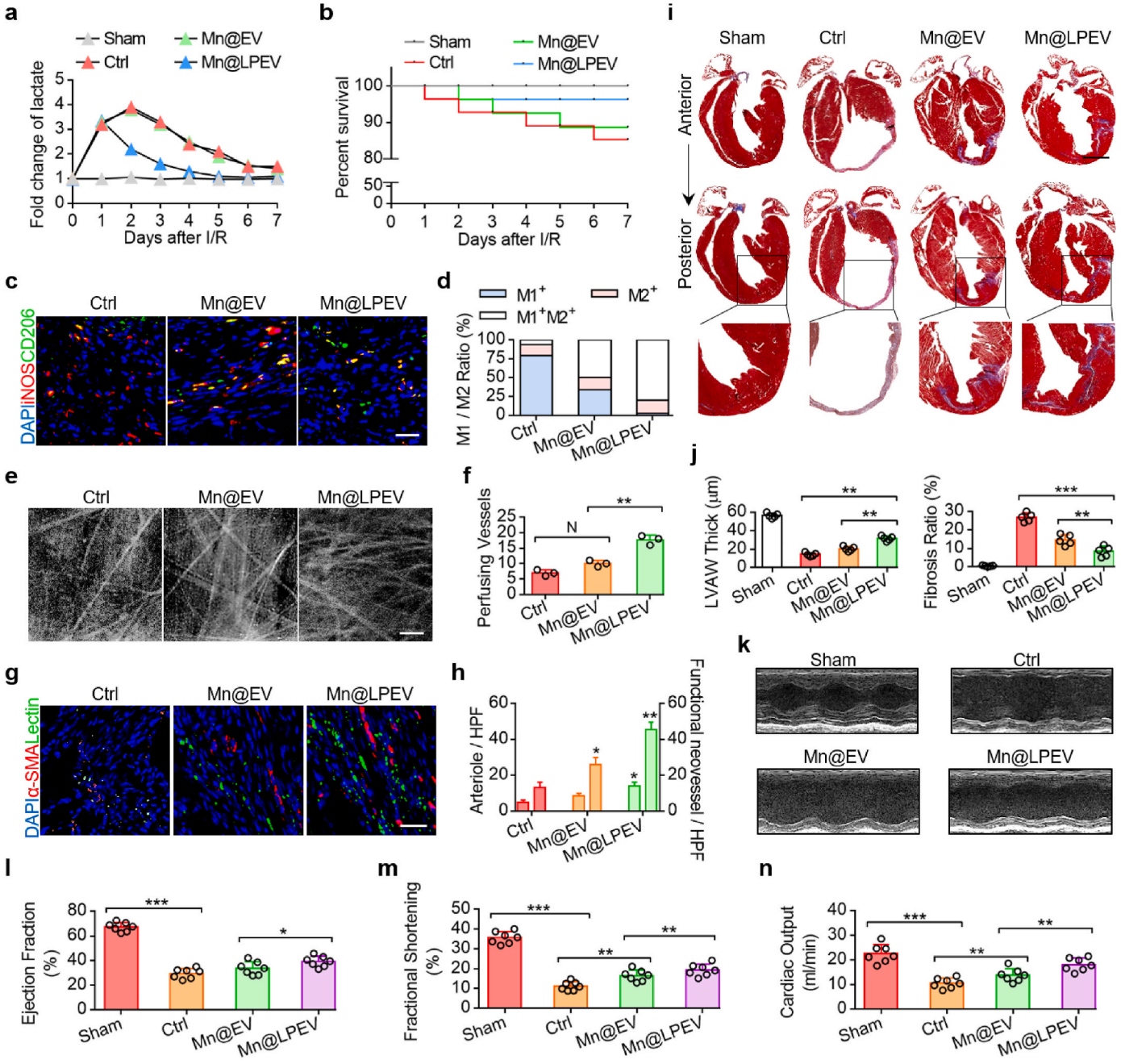

Fig. 5. Mn@LPEV detoxifies lactate, facilitates heart repair and function recovery. a, b) In the first week after I/R and treatments, heart tissue lactate was measured (a) and mice death was recorded by survival curve (b). c, d) M1 and M2 macrophages was identified and quantified by iNOS and CD206 respectively 7-day after treatments. Red, iNOS; Green, CD206. bar = 10 μm, n = 5. e, f) After i.v injection of fluorescein sodium, mice hearts were directly observed under IVCS to assess LVAW microcirculation perfusion 4w after treatments. bar = 1 mm. g, h) Small arterioles and functional neovessels were identified by α-SMA and i.v. injected Lectin, and further quantified. Red, α-SMA; Green, Lectin. bar = 50 μm, n = 5. i, j) Fibrosis remodeling of heart tissues was assessed by Masson staining (i), and the LVAW thickness (j, left) and fibrosis ratio (j, right) were further measured. bar = 50 μm, n = 5. k-n) Echocardiography (k) was used to assess heart function (l, EF; m, FS; n, CO) after treatments. n = 7. *p < 0.05, **p < 0.01, ***p < 0.001, N = non-significant.

the efficacy of the artificial peroxisome in alleviating myocardial DDR and promoting regeneration after I/R. The active delivery system, which is platelet biomimetic and lactate-responsive significantly enhanced these effects.

2.7. Mn@LPEV detoxifies lactate and facilitates heart repair and function recovery

One week after I/R and treatment, we investigated tissue lactate level and found that only the artificial peroxisome Mn@LPEV effectively detoxified the accumulated lactate, highlighting the substrate-oxidizing function of the biomimetic Mn@LPEV (Fig. 5a). During which, mice mortality rate was also recorded and demonstrated the mortality-reducing effects of lactate-catalyzing Mn@LPEV (Fig. 5b). Together with the above results, these findings indicate that our artificial peroxisome Mn@LPEV successfully mimicked peroxisome to maintain cardiac redox homeostasis after I/R. We then examined heart sections to investigate the inflammatory response. Mn@LPEV significantly decreased the population of inflammatory M1 macrophages and increased reparative M2 macrophages (Fig. 5c and d), indicating the immunomodulation for macrophage polariton by our biomimetic peroxisome. To evaluate heart perfusion and microcirculation, we observed the heart's microcirculation using an in vivo confocal system (IVCS) and confirmed neovascularization following Mn@LPEV therapy (Fig. 5e and f). Additionally, we stained α-SMA after i.v. administrated Lectin to indicate microarteries and functional neovessels [20], and revealed significant increase both in arterioles density and neovessels as for the treatment of MSC-EV-original Mn@LPEV (Fig. 5g and h).

The fibrosis remodeling of myocardium was further investigated using Masson's trichrome staining, which demonstrated that Mn@LPEV significantly preserved left ventricular anterior wall (LVAW) thickness and reduced fibrosis volume compared to control and Mn@EV therapies (Fig. 5i and j). Finally, we assessed mice cardiac function by echocardiography. As shown in Fig. 5k–n, the biomimetic peroxisome Mn@LPEV preserved heart function better than Mn@EV, as indicated by ejection fraction (EF) (38.9 % vs. 33.8 % vs. 29.6 % for Mn@LPEV, Mn@EV and Ctrl, respectively) and fractional shortening (FS) (19.4 % vs. 15.9 % vs. 11.3 % for Mn@LPEV, Mn@EV and Ctrl, respectively) and cardiac output (CO) (17.9 mL/min vs. 13.8 mL/min vs. 10.5 mL/min for Mn@LPEV, Mn@EV and Ctrl, respectively). Overall, our biomimetic peroxisome Mn@LPEV demonstrated therapeutic effects in preventing acute death, modulating inflammation, promoting angiogenesis, reducing fibrosis, and protecting heart function.

2.8. Biosafety assessment

To assess the biosafety of our biomimetic peroxisome before clinical application, we initially performed apoptosis indicator caspase-3 immunohistochemistry (IHC) staining to investigate histological changes in various organs. No apparent toxic damage was observed across the different treatment groups (Fig. S6a). In clinical settings, heart attacks often follow the formation of microthrombi in the coronary arteries. To evaluate the thrombogenic risk of these treatments, we performed a platelet aggregation test. When preincubated with Mn@LPEV and stimulated by thrombin, platelets reached a maximum aggregation of 86 % showing no significant differences compared to the control or Mn@EV groups (Figs. S6b and c), suggesting a minimal influence on platelet function. In addition, the blood clotting function test confirmed the satisfactory safety regarding thrombus risk (Fig. S6d). Finally, we measured biochemistry criteria after treatments and found that these treatments did not have a significant impact on these indicators (Fig. S6e).

3. Conclusion and discussion

Through Mn_3O_4 and LOX, we fabricated an MSC-EV-based artificial peroxisome to maintain redox homeostasis in the stressed myocardium. This artificial peroxisome mimicked both the peroxidase and oxidase activities of natural peroxisomes in scavenging ROS and lactate, effectively inhibiting the DDR pathway which in turn reactivated the myocardial cell cycle and promoted proliferation. Enabled by the platelet biomimetic and lactate-responsive delivery strategy, the biomimetic peroxisome could actively target heart injuries, and promote heart repair and regeneration in I/R mice. This included immunomodulation, proangiogenesis, reduction in mortality and fibrosis, as well as myocardial regeneration and functional recovery.

Regarding above results of our therapy in promoting heart regeneration, however, the mechanisms following the DDR should be further addressed. For example, latest literatures have revealed that lipid metabolism is strongly associate with the myocardial cell cycle and proliferation. Fatty acid oxidation is detrimental to myocardial proliferation and control cell cycle arrest by an epigenetic modification of histones, while sphingolipid metabolism can promote mammalian heart regeneration through inhibiting the deacetylation of H3K9/H3K27 and increasing transcription levels of ErbB4, MEF2A and MEF2C. However, both of above-mentioned lipid substrates are related to mitochondrial oxidation and might be strongly linked to the DNA response and cell-cycle control. This needs further identification of crosslink between DDR and lipid metabolism-associated epigenetic modification of histone.

The drug loading by EV have achieve advances but still being challenged by some limitations, particularly the loading efficiency [31]. In this study, we loaded nanozymes into MSC-EV by pretreating MSC with Mn_3O_4, and the vesicle membrane can further load drugs by a piggy-back strategy, which can be implemented for extend therapeutics. Respecting to limitations of this study, however, we have not reached a method to address how many drugs were loaded in the EV, which need future efforts to explore not only for the nanozymes, but also these unquantifiable drugs. But, despite all this, we established a strategy to mimic the peroxisome and demonstrated a way to target myocardial DDR and regenerate the heart.

4. Methods and materials

4.1. Materials preparation and fabrication of biomimetic peroxisome Mn@LPEV

The Mn_3O_4 nanozyme was synthesized using our previous thermal decomposition method [23] and is briefly described in the supporting information. Rat bone marrow MSCs were maintained under standard conditions [20,21], and were cocultured with Mn_3O_4 (0.1 mg/mL) for 48 h before collecting culture medium, that was first centrifugated (500g*10min) to remove cells and cell debris, and then ultra-centrifugated (100000g*45min) to isolate Mn_3O_4-loaded MSC-EV (Mn@EV) [32,33]. The Mn@EV examples were further ultrafiltrated through a Millipore (0.05 μm) to exclude free Mn_3O_4. Platelet membrane vesicles (PMVs) were obtained from freshly collected platelets using a freeze-thaw method, and then fused with Mn@EV (1:1, protein wight) via sonication and extrusion [21,34] to produce platelet biomimetic vesicles (Mn@PEV). Lactate oxidase was stirred with DSPE-PEG-NHS to create DSPE-PEG-LOX conjugates. Finally, the biomimetic peroxisome Mn@LPEV was fabricated by modifying Mn@PEV with DSPE-PEG-LOX conjugates (2 %), via sonication 2 min and following ultrafiltration to exclude free LOX [30,35]. These formulations were subsequently characterized using Western blot (WB), confocal, TEM and DLS techniques, etc.

4.2. The antioxidative and pro-proliferative activity of Mn@LPEV in vitro

Cardiomyocytes extracted from P1, P7 neonatal C57BL/6 mice were treated with 100 μM H_2O_2 or subjected to hypoxia/reoxygenation (H/R) to induce oxidative stress. Concurrently, the cells were cultured with

Mn_3O_4, Mn@EV, or Mn@LPEV for 12 h. The antioxidative and mitochondrial protective effects of these treatments were assessed using various probes, including mitoSOX (Invitrogen), DCFH-DA (Beyotime, China), Calcein AM (Cal AM, beyotime, China) and TMRM (Invitrogen). DNA damage and DDR activation were evaluated by measuring the base modification maker 8-OHdG (Invitrogen) and pATM (Invitrogen). Proteins involved in the cell cycle, such as Wee1 (Abcam), pH3, (Huabio, China) and Ki67 (Invitrogen), were analyzed through WB or IF. Additionally, cell mitosis was quantified by identifying Auro B via IF.

4.3. Active binding and targeting experiments

HUVEC cells were exposed to oxidative stress using 100 μM H_2O_2 for 10 h. After washing, the cells were incubated with 5 μg/mL DiD-labeled Mn@EV or Mn@LPEV at 4 °C for 10 min. A motion tracking system was set up with a microscope [21], where one side chamber contained lactate medium and the other side contained control medium. The middle chamber was filled with Mn@PEV or Mn@LPEV. In the Transwell assay, HUVECs and H9C2 cells were maintained in the upper and lower chambers, respectively under treatment with H_2O_2. The medium in the upper chamber was then refreshed with DiD-labeled Mn@PEV or Mn@LPEV. Subsequently, the internalization of these vesicles was observed and quantified. In vivo, 24 h after I/R operation, mice were intravenously injected with 200 μl of DiR-labeled Mn@EV, Mn@LPEV, or PBS. The targeting of these formulations to mouse hearts was investigated 2h post-administration using the IVIS system and immunohistochemistry with anti-cTnT (Abcam). Additionally, their distribution in major organs, including the liver, spleen, lung, kidney, and brain, was also quantified.

4.4. Laboratory animal and treatment assignment

C57BL/6 mice (20 g ± 2 g) were obtained from the Sir Run Shaw Hospital Animal Experiment Center, Ltd. All animal experiments were conducted with the approval of the Ethics Committee of Sir Run Shaw Hospital (SRRSH202302225), Zhejiang University. Myocardial I/R injury was induced in mice by ligating the left anterior descending coronary artery for 45 min, followed by reperfusion. The mice were then randomized into four groups to receive different treatments: sham (mice with a sham operation), control (saline), and either Mn@EV or Mn@LPEV (i.v, 20 μg/200 μL), administered at 1, 2, and 3 days post-operation.

4.5. Cardiomyocyte DDR and proliferation assessment in vivo

One week after treatments, myocardial oxidative stress was evaluated by measuring tissue ROS using DHE (Beyotime) and observing mitochondrial morphology. Cell apoptosis was assessed using Tunel assay (Abcam). DNA damage and the DDR were indicated by the levels of 8-OHdG and pATM respectively. Subsequently, heart samples were collected 28 days post-treatment to evaluate cardiac proliferation. initially, the ratios of heart weight to body weight and heart weight to tibia length were measured. WGA staining (Thermo Fisher) was then performed to compare cardiomyocyte size and number. Finally, pH3 and Ki67 staining were used to assess myocardial proliferation.

4.6. Cardiac repair and function assessment

In the first week following I/R, daily measurements of heart tissue lactate were performed on the mice. Mortality was quantified by recording survival curves. Seven days after treatments, the presence of M2 macrophages was identified using CD206 (Abcam) to evaluate the immunomodulatory effects of the therapies. Four weeks after treatment, micro-vessel, and microcirculation perfusion were assessed using Lectin, α-SMA (Abcam) staining and IVCS (MR-solution, France), respectively. Subsequently, hearts were harvested, sectioned, and subjected to Masson's trichrome staining. The collagen area and percentage were analyzed using ImageJ software. Finally, transthoracic echocardiography (Visual Sonics Vevo 770 system) was performed on mice to evaluate cardiac function by calculating alterations in left ventricular ejection fraction (LVEF), left ventricular fractional shortening (LVFS), and cardiac output (CO) based on M-mode traces from six consecutive cardiac cycles.

4.7. Statistical analysis

Data are expressed as the mean ± SD. Statistical analyses were performed using GraphPad Prism (version8.0). Two-group comparisons were conducted using a two-tailed unpaired Student's t-test. For comparisons involving more than two groups, one-way analysis of variance (ANOVA) was employed. Statistical significance was defined as $p < 0.05$.

CRediT authorship contribution statement

Ning Zhang: Writing – review & editing, Visualization, Validation, Supervision, Project administration, Methodology, Conceptualization. **Menghan Gao:** Investigation, Formal analysis. **Xiaolong Hu:** Investigation, Formal analysis, Data curation. **Peng Wang:** Investigation. **Yuan Cheng:** Resources, Methodology. **Hui Wei:** Resources, Methodology. **Guosheng Fu:** Project administration. **Junbo Ge:** Resources. **Hongjun Li:** Resources, Methodology, Conceptualization. **Wenbin Zhang:** Validation, Supervision, Resources. **Binquan Zhou:** Validation, Supervision, Resources.

Declaration of competing interest

The authors declare that they have no known competing financial interests or personal relationships that could have appeared to influence the work reported in this paper.

Acknowledgements

Ning Zhang, XL Hu, and MH Gao contributed equally to this work. This work was partially supported by the National Natural Science Foundation of China (82300565, 8217020192), and by the Natural Science Foundation of Zhejiang Province (LQ24H020005), Medical Science and Technology Project of Zhejiang Province (2024KY108), Zhejiang Province Postdoctoral Special Research Project of China (ZJ2023069).

Appendix A. Supplementary data

Supplementary data to this article can be found online at https://doi.org/10.1016/j.biomaterials.2025.123214.

Data availability

Data will be made available on request.

References

[1] H. Tian, X. Zhao, Y. Zhang, Z. Xia, Abnormalities of glucose and lipid metabolism in myocardial ischemia-reperfusion injury, Biomed. Pharmacother. 163 (2023) 114827.
[2] C.J. Zuurbier, L. Bertrand, C.R. Beauloye, I. Andreadou, M. Ruiz-Meana, N. R. Jespersen, D. Kula-Alwar, H.A. Prag, H. Eric Botker, M. Dambrova, C. Montessuit, T. Kaambre, E. Liepinsh, P.S. Brookes, T. Krieg, Cardiac metabolism as a driver and therapeutic target of myocardial infarction, J. Cell Mol. Med. 24 (11) (2020) 5937–5954.
[3] Y. Wu, N. Huang, T. Sun, B. Zhang, S. Zhang, P. Zhang, C. Zhang, Association between normalized lactate load and in-hospital mortality in patients with acute myocardial infarction, Int. J. Cardiol. 399 (2024) 131658.

[4] J. Takahashi, A. Suda, S. Yasuda, H. Shimokawa, Measurement of myocardial lactate production for diagnosis of coronary microvascular spasm, J. Vis. Exp. 175 (2021).
[5] D.A. Duse, M. Kelm, R. Erkens, Lactate load in acute myocardial infarction: old but gold? Int. J. Cardiol. 399 (2024) 131771.
[6] B.N. Puente, W. Kimura, S.A. Muralidhar, J. Moon, J.F. Amatruda, K.L. Phelps, D. Grinsfelder, B.A. Rothermel, R. Chen, J.A. Garcia, C.X. Santos, S. Thet, E. Mori, M.T. Kinter, P.M. Rindler, S. Zacchigna, S. Mukherjee, D.J. Chen, A.I. Mahmoud, M. Giacca, P.S. Rabinovitch, A. Aroumougame, A.M. Shah, L.I. Szweda, H.A. Sadek, The oxygen-rich postnatal environment induces cardiomyocyte cell-cycle arrest through DNA damage response, Cell 157 (3) (2014) 565–579.
[7] E.R. Porrello, A.I. Mahmoud, E. Simpson, J.A. Hill, J.A. Richardson, E.N. Olson, H. A. Sadek, Transient regenerative potential of the neonatal mouse heart, Science (New York, N.Y.) 331 (6020) (2011) 1078–1080.
[8] W. Kimura, F. Xiao, D.C. Canseco, S. Muralidhar, S. Thet, H.M. Zhang, Y. Abderrahman, R. Chen, J.A. Garcia, J.M. Shelton, J.A. Richardson, A.M. Ashour, A. Asaithamby, H. Liang, C. Xing, Z. Lu, C.C. Zhang, H.A. Sadek, Hypoxia fate mapping identifies cycling cardiomyocytes in the adult heart, Nature 523 (7559) (2015) 226–230.
[9] S.E. Senyo, M.L. Steinhauser, C.L. Pizzimenti, V.K. Yang, L. Cai, M. Wang, T.D. Wu, J.L. Guerquin-Kern, C.P. Lechene, R.T. Lee, Mammalian heart renewal by pre-existing cardiomyocytes, Nature 493 (7432) (2013) 433–436.
[10] Y. Nakada, D.C. Canseco, S. Thet, S. Abdisalaam, A. Asaithamby, C.X. Santos, A. M. Shah, H. Zhang, J.E. Faber, M.T. Kinter, L.I. Szweda, C. Xing, Z. Hu, R. J. Deberardinis, G. Schiattarella, J.A. Hill, O. Oz, Z. Lu, C.C. Zhang, W. Kimura, H. A. Sadek, Hypoxia induces heart regeneration in adult mice, Nature 541 (7636) (2017) 222–227.
[11] I. Menendez-Montes, D.J. Garry, J.J. Zhang, H.A. Sadek, Metabolic control of cardiomyocyte cell cycle, Methodist DeBakey cardiovascular journal 19 (5) (2023) 26–36.
[12] K. Okumoto, S. Tamura, M. Honsho, Y. Fujiki, Peroxisome: metabolic functions and biogenesis, Advances in experimental medicine and biology 1299 (2020) 3–17.
[13] R. Ravindran, I.O.L. Bacellar, X. Castellanos-Girouard, H.M. Wahba, Z. Zhang, J. G. Omichinski, L. Kisley, S.W. Michnick, Peroxisome biogenesis initiated by protein phase separation, Nature 617 (7961) (2023) 608–615.
[14] S. Gaussmann, R. Peschel, J. Ott, K.M. Zak, J. Sastre, F. Delhommel, G. M. Popowicz, J. Boekhoven, W. Schliebs, R. Erdmann, M. Sattler, Modulation of peroxisomal import by the PEX13 SH3 domain and a proximal FxxxF binding motif, Nat. Commun. 15 (1) (2024) 3317.
[15] J. Wu, X. Wang, Q. Wang, Z. Lou, S. Li, Y. Zhu, L. Qin, H. Wei, Nanomaterials with enzyme-like characteristics (nanozymes): next-generation artificial enzymes (II), Chem. Soc. Rev. 48 (4) (2019) 1004–1076.
[16] R. Yuan, Y. Li, S. Han, X. Chen, J. Chen, J. He, H. Gao, Y. Yang, S. Yang, Y. Yang, Fe-curcumin nanozyme-mediated reactive oxygen species scavenging and anti-inflammation for acute lung injury, ACS Cent. Sci. 8 (1) (2022) 10–21.
[17] N. Singh, G.R. Sherin, G. Mugesh, Antioxidant and prooxidant nanozymes: from cellular redox regulation to next-generation therapeutics, Angew Chem. Int. Ed. Engl. 62 (33) (2023) e202301232.
[18] X. Liu, B. Chen, J. Chen, X. Wang, X. Dai, Y. Li, H. Zhou, L.M. Wu, Z. Liu, Y. Yang, A cardiac-targeted nanozyme interrupts the inflammation-free radical cycle in myocardial infarction, Advanced materials (Deerfield Beach, Fla.) 36 (2) (2024) e2308477.
[19] P. Menasche, Cell therapy trials for heart regeneration - lessons learned and future directions, Nat. Rev. Cardiol. 15 (11) (2018) 659–671.
[20] N. Zhang, Y. Song, Z. Huang, J. Chen, H. Tan, H. Yang, M. Fan, Q. Li, Q. Wang, J. Gao, Z. Pang, J. Qian, J. Ge, Monocyte mimics improve mesenchymal stem cell-derived extracellular vesicle homing in a mouse MI/RI model, Biomaterials 255 (2020) 120168.
[21] N. Zhang, M. Fan, Y. Zhao, X. Hu, Q. Zhu, X. Jiao, Q. Lv, D. Li, Z. Huang, G. Fu, J. Ge, H. Li, W. Zhang, Biomimetic and NOS-responsive nanomotor deeply delivery a combination of MSC-EV and mitochondrial ROS scavenger and promote heart repair and regeneration, Adv. Sci. 10 (21) (2023) e2301440.
[22] J. Yao, Y. Cheng, M. Zhou, S. Zhao, S. Lin, X. Wang, J. Wu, S. Li, H. Wei, ROS scavenging Mn(3)O(4) nanozymes for in vivo anti-inflammation, Chem. Sci. 9 (11) (2018) 2927–2933.
[23] Y. Cheng, C. Cheng, J. Yao, Y. Yu, Y. Liu, H. Zhang, L. Miao, H. Wei, Mn3O4 nanozyme for inflammatory bowel disease therapy, Adv. Therapeut. 4 (9) (2021) 2100081.
[24] Y. Song, N. Zhang, Q. Li, J. Chen, Q. Wang, H. Yang, H. Tan, J. Gao, Z. Dong, Z. Pang, Z. Huang, J. Qian, J. Ge, Biomimetic liposomes hybrid with platelet membranes for targeted therapy of atherosclerosis, Chem. Eng. J. (2020) 127296.
[25] C. Chen, Y. Zhang, Z. Chen, H. Yang, Z. Gu, Cellular transformers for targeted therapy, Adv. Drug Deliv. Rev. 179 (2021) 114032.
[26] Z. Zhao, Y. Yang, T. Sheng, Y. Bao, R. Yu, X. Yu, S. Jia, Q. Wu, C. Zhu, X. Shen, W. Zhang, Z. Lu, K. Ji, X. Chen, X. Jiang, Y. Zhang, Z. Gu, J. Yu, Platelet-drug conjugates engineered via one-step fusion approach for metastatic and postoperative cancer treatment, Angew. Chem. Int. Ed. n/a(n/a) e202403541.
[27] J. Tang, T. Su, K. Huang, P. Dinh, Z. Wang, A. Vandergriff, M. Hensley, J. Cores, T. Allen, T. Li, E. Sproul, E. Mihalko, L. Lobo, L. Ruterbories, A. Lynch, A. Brown, T. Caranasos, D. Shen, G. Stouffer, Z. Gu, J. Zhang, K. Cheng, Targeted repair of heart injury by stem cells fused with platelet nanovesicles, Nat. Biomed. Eng. 2 (2018) 17–26.
[28] D.C. Canseco, W. Kimura, S. Garg, S. Mukherjee, S. Bhattacharya, S. Abdisalaam, S. Das, A. Asaithamby, P.P. Mammen, H.A. Sadek, Human ventricular unloading induces cardiomyocyte proliferation, J. Am. Coll. Cardiol. 65 (9) (2015) 892–900.
[29] L. Wu, J.R. Sowers, Y. Zhang, J. Ren, Targeting DNA damage response in cardiovascular diseases: from pathophysiology to therapeutic implications, Cardiovasc. Res. 119 (3) (2022) 691–709.
[30] Z. Zhang, H. Zhong, Y. Zhou, P. Ke, Q. Dai, Y. Lu, X. Zhong, Q. Yang, Y. Xia, X. Bao, L. Wu, M. Han, J. Gao, Lactate-driving Pt nanoflower with positive chemotaxis for deep intratumoral penetration, Nano Today 45 (2022) 101542.
[31] P. Vader, E.A. Mol, G. Pasterkamp, R.M. Schiffelers, Extracellular vesicles for drug delivery, Adv. Drug Deliv. Rev. 106 (Pt A) (2016) 148–156.
[32] G. Chen, D. Jiang, S. Ding, C. Huang, D. Zhu, H. Jiang, A tumor cell exosome-mimicking multifunctional nanozyme for targeted breast cancer radiotherapy, Nanoscale 15 (36) (2023) 14949–14957.
[33] J.R. Lee, B.W. Park, J. Kim, Y.W. Choo, H.Y. Kim, J.K. Yoon, H. Kim, J.W. Hwang, M. Kang, S.P. Kwon, S.Y. Song, I.O. Ko, J.A. Park, K. Ban, T. Hyeon, H.J. Park, B. S. Kim, Nanovesicles derived from iron oxide nanoparticles-incorporated mesenchymal stem cells for cardiac repair, Sci. Adv. 6 (18) (2020) eaaz0952.
[34] Y. Zhou, Q. Liang, X. Wu, S. Duan, C. Ge, H. Ye, J. Lu, R. Zhu, Y. Chen, F. Meng, L. Yin, siRNA delivery against myocardial ischemia reperfusion injury mediated by reversibly camouflaged biomimetic nanocomplexes, Advanced materials (Deerfield Beach, Fla.) 35 (23) (2023) e2210691.
[35] H. Di, E. Zeng, P. Zhang, X. Liu, C. Zhang, J. Yang, D. Liu, General approach to engineering extracellular vesicles for biomedical analysis, Anal. Chem. 91 (20) (2019) 12752–12759.